CHEMISTRY OF MATERIALS

Article

A chemical understanding for the band convergence in thermoelectric CoSb3 skutterudites: influence of electron population, local thermal expansion and bonding interactions

Riley Hanus, Xingyu Guo, Yinglu Tang, Guodong Li, G. Jeffrey Snyder, and Wolfgang G. Zeier

Chem. Mater., **Just Accepted Manuscript** • DOI: 10.1021/acs.chemmater.6b04506 • Publication Date (Web): 01 Jan 2017

ACS Publications

Chemistry of Materials is published by the American Chemical Society. 1155 Sixteenth Street N.W., Washington, DC 20036

A chemical understanding for the band convergence in thermoelectric $CoSb_3$ skutterudites: influence of electron population, local thermal expansion and bonding interactions

Riley Hanus[a], Xingyu Guo[a], Yinglu Tang[b], Guodong Li[c],
G. Jeffrey Snyder[a*], Wolfgang G. Zeier[d*]

[a]Department of Materials Science and Engineering, Northwestern University, Evanston IL 60208, USA

[b]EMPA, Swiss Federal Laboratories for Materials Science and Technology, Laboratory for Energy Conversion, 8600 Dübendorf, Switzerland

[c]School of Science, Wuhan University of Technology, Wuhan, China

[d]Physikalisch-Chemisches Institut, Justus-Liebig-University Gießen, Heinrich-Buff-Ring 17, 25392 Giessen, Germany

Abstract

N-type skutterudites, such as $Yb_xCo_4Sb_{12}$, have recently been shown to exhibit high valley degeneracy with possible band convergence, explaining the excellent thermoelectric efficiency in these materials. Using a combined theoretical and experimental approach involving temperature-dependent synchrotron diffraction, molecular orbital diagrams and computational studies, the chemical nature of critical features in the band structure are highlighted. We identify how n-type doping on the filler site induces structural changes that are observed in both the diffraction data and computational results. Additionally, we show how chemical n-type doping slightly alters the electronic band structure moving the high valley degeneracy secondary conduction band closer to the primary conduction band and thus inducing band convergence.

1. Introduction

Engineering the electronic band structure of a material is an effective method for improving thermoelectric efficiency, as it increases the band degeneracy near the Fermi level, which is directly proportional to the quality factor of thermoelectric materials[1–4]. For instance, in PbTe and SnTe materials the two valence bands converge at higher temperatures, which significantly increases the power factor and ultimately the zT. The convergence of these bands occurs because of an increasing off-centering displacement of Pb with temperature[5], leading to a decreasing lone-pair s^2 dominated valence band[6]. The possibility of changing band convergence behavior through replacing Pb with non-lone-pair containing elements shows how important the local chemical bonding environment is in a thermoelectric material[7–10]. Further examples for the influence of crystal chemistry on the electronic bands and band convergence has been shown for chalcopyrites, Mg_2Sn and have even been predicted for Zintl phases[2,11–14]. As the band convergence in these materials has shown, a materials band structure is deeply linked to the underlying nature of its chemical bonds. Therefore, changing bonding interactions is the most effective approach at engineering the band degeneracy of thermoelectric materials.

Skutterudite $CoSb_3$ is a well-known thermoelectric material, but only recently has it been shown that, when heavily doped[15], it exhibits a complex Fermi surface with multiple valleys. Indeed, the extraordinary electronic properties of *n*-type thermoelectric $CoSb_3$ originates from the presence of a multi-valley secondary conduction band (CB_2) located between the Γ and N points, which is somewhat higher in energy compared to the primary, Γ-point conduction band (CB_Γ). For highly doped samples and at elevated temperatures (~700K), CB_2 appears to contribute substantially to the thermoelectric performance possibly even converging with (having the same energy as) the primary conduction band at Γ.

Inspired by the underlying chemical reasons for band convergence in PbTe, in this study we aim to understand the observed band convergence in $CoSb_3$ from a chemical point of view. In this work, we use a combination of temperature dependent synchrotron diffraction and density functional theory calculations, in which the obtained structural data is used as an input for the theoretical calculations. The diffraction data reveals differences in the coefficient of thermal expansion of local bonds within the structure (*local*-CTE). These structural parameters are employed in the calculations to assess changes in the band structure due to structural changes. These experimental and computational efforts identify the chemical nature of the primary (CB_Γ) and secondary (CB_2) conduction bands. We then show both experimentally and computationally how Yb doping changes the $CoSb_3$ structure beyond simple lattice expansion. Furthermore, a slight structure change observed with increasing Fermi level demonstrates a coupling of these conduction band states to the atom positions. It is also shown that this increase in Fermi level induces band convergence in $CoSb_3$ at room temperature and above. Here, we show that band convergence can be chemically induced through population of conduction band states not expected from a rigid band model.

2. Experimental and Computational Methods

The combined experimental and computational approach is described in detail below. Synthesis of the samples was performed using the method given by Tang *et al.*[15]

Powder Diffraction. X-ray powder diffraction was conducted at Argonne National Lab Advanced Photon Source (APS) on the designated powder diffraction beam line; 11-BM. Standard Debye-Scherrer geometry with a 1D detector was used for the experiment and the calibrated X-ray wavelength was 0.414208 Å. An Al_2O_3/Si reference sample was used for alignment and an instrument parameter file was obtained using a LaB_6 standard (specifics about profile parameters are given below in the refinement section). Sample absorption was calculated using the ABSORB web utility[17] (which uses the Cromer & Liberman algorithm to compute X-ray scattering cross sections[18]). After optimizing the absorption factor, quartz capillary diameters of 0.4 mm and 0.3 mm were used for powder samples of $CoSb_3$ and $Yb_{0.3}Co_4Sb_{12}$, respectively (no diluting media was necessary). The same anomalous scattering parameters, f' and f'', used for the absorption calculation were also used in the Rietveld refinements. Room temperature scans of both samples were conducted using a high-speed sample spinner (~90 Hz). High temperature scans from 100 °C to 500 °C with 100 °C steps were conducted using the Cyberstar hot air blower with its corresponding sample spinner (~20Hz). A typical intensity for the primary diffraction peak was ~300,000 counts for the 300 K scans and ~200,000 counts for the scans at elevated temperature, confirming the quality of the data.

Refinements. To examine structural changes of $CoSb_3$ with temperature and doping, Rietveld refinements were conducted on the temperature dependent, high-resolution, powder diffraction data of filled and unfilled $CoSb_3$. Refinements were conducted using the General Structure Analysis System (GSAS[19,20]) for $CoSb_3$ in the $Im\overline{3}$ space group with Co atoms at (0.25, 0.25, 0.25), and Sb atoms at (0, *y*, *z*). In this representation, the filler atom is located at (0, 0, 0). Note that the origin in *Figure 1* is shifted to effectively show both Sb-Sb long and short bonds in one figure. LaB_6 powder was used to construct an instrument parameter file and a pseudo-Voigt peak profile was used (CW profile function 3 in GSAS). The peak profile parameters from this LaB_6 parameter file were fixed throughout the refinement procedure until the last refinement step in which all refinement parameters were unfixed and refined together. To account for peak anisotropy seen in the $Yb_{0.3}Co_4Sb_{12}$ sample, anisotropic peak broadening parameters were included through the γ-profile function (L11, L22, etc. parameters in GSAS) in these refinements. Refinements of $Yb_{0.3}Co_4Sb_{12}$ without the anisotropic profile parameters were also conducted and the same trends were concluded for structural changes with temperature and doping, however the peak positions were more accurately represented when anisotropic profile parameters were included and these results are reported here. In all diffraction histograms, the electron density on the Co site (0.25, 0.25, 0.25) was slightly larger relative to that on the Sb site (0, *y*, *z*). Several defect mechanisms were tested and statistically equivalent refinements were achieved for anti-site disorder of Sb on the Co site as well as Sb vacancies. As Sb vacancies would introduce electrons, and since the undoped samples are slightly n-type[15], a slight Sb deficiency is assumed. To include Sb vacancies in the refinement, the Co occupancy was set to 100% and the Sb occupancy was refined along with the scaling parameter. Note that a high frequency sample spinner was used for the room temperature scans resulting in better counting statistics than the scans at elevated temperatures in which a lower frequency sample spinner was used. This is reflected in the refinement statistics, in which the room temperature refinements have a higher χ^2 due to better counting statistics. Refinement uncertainties are given in the tabulated diffraction data in the Supporting Information and the experimental uncertainty of the lattice parameters of beam line 11-BM is 0.0001 Å.

Computational methods. Density-functional theory (DFT) calculations for both doped and undoped $CoSb_3$ were conducted to determine how changes in structure and Fermi level will affect the electronic band structure.

We performed all DFT calculations as implemented in the Vienna *ab initio* simulation package (VASP) code. The projector-augmented wave (PAW) method[21] with Perdew-Burke-Ernzerhof (PBE) exchange-correlation functional were used for calculations on the primitive unit cell and the Yb-doped supercell[22]. The unit cell structure was fully relaxed with a plane wave cutoff energy of 550 eV with a Gamma centered 7x7x7 Monkhorst-Pack uniform *k*-point reciprocal space sampling. The 0.01 eV/Å Hellmann-Feynman forces were adopted for geometry optimization. The optimized lattice parameter is found to be 9.11 Å, which is consistent with the previous theoretical value of 9.115 Å using PBE[23], and the internal parameters u=0.3333, v=0.1595. The calculated direct band gap of $CoSb_3$ is 0.1665 eV, which agrees well with the gap of 0.17 eV reported earlier[24]. Sofo *et al.* reported a slightly higher value of 0.22 eV[25]. After our calculations of the fully relaxed $CoSb_3$ were validated with previous calculations and literature values, a systematic study on how crystal structure and doping effect the band structure was conducted.

The structural parameters of $CoSb_3$ and $Yb_{0.3}Co_4Sb_{12}$ from 300 to 800 K, as determined via synchrotron diffraction, were used to calculate band structures. In this way, a '0 K' calculation is conducted with structural parameters set to their values at a given temperature (300 to 800 K) and we refer to this, here, as the band structure at that specific temperature. This method neglects the contribution of lattice vibrations, meaning that the computations with temperature only probe the influence of structure change on the band structure. In reality, there is an additional contribution from lattice vibrations through electron-phonon interactions (e.g. see Figure 1 of Gibbs *et. al*.[26]). The room temperature band gap of $CoSb_3$ calculated by this method is 0.1625 eV, which agrees with room temperature optical absorption measurements[15].

Here, all calculations of Yb-doped $CoSb_3$ were performed in a 2x2x2 supercell which contains 130 atoms. The chemical composition of this supercell is $Yb_{0.25}Co_4Sb_{12}$. The nominal composition of the doped $CoSb_3$ is $Yb_{0.3}Co_4Sb_{12}$ and the occupancy from refinements show that the Yb content is slightly lower than the nominal content, suggesting that this composition is close to that observed experimentally[15]. Again, the atomic positions were fixed to that measured from synchrotron diffraction. Typically, the atomic positions are relaxed in supercell calculations as the positions near an impurity atom will be different than the atomic positions away from one. Synchrotron diffraction and Rietveld analysis give a spatial average of the atomic positions. Because of this, fixing the atomic positions to the spatial average may be unphysical and skew the computational results. DFT calculations, where the lattice parameter was set and the ion-positions are relaxed, were conducted to ensure that the observed trends were not artifacts of the method in which the supercell calculations were conducted. Additionally, calculations in which the Fermi level was intentionally shifted were conducted to deduce how changing the carrier concentration will affect the band structure (summary provided in Supplemental Information) in addition to the calculations discussed in Section 3.2. This was achieved by manually increasing the number of electrons of $CoSb_3$, as well as conducting charged impurity calculations where Yb_i^{2+} was included and compared to the calculation with Yb_i^0. A compensating background charge was included, in these, to prevent divergence of the total energy of the charged system.

The COHP were generated by transferring the PAW wave functions to properly chosen local basis with Local Orbital Basis Suite Towards Electronic-Structure Reconstruction (LOBSTER) code[27], and the band unfolding procedure for Yb-doped $CoSb_3$ supercell was performed using the BandUP code[28].

3. Results and Discussion

3.1 Temperature dependent structural changes in $CoSb_3$

Figure 1 shows a structural representation of a filled $CoSb_3$ skutterudite. For a more in-depth structural discussion, the reader is referred to a review by Uher[29]. In brief, in $CoSb_3$ Sb forms polyanionic Sb_4 rings. Using a Zintl description, each Sb has a formal charge of

-1 forming two covalent bonds and giving the ring a formal charge of Sb_4^{4-}. The Sb_4 ring itself is not necessarily a square, having two longer and two shorter bonds of a rectangle. The remaining two Sb lone pairs coordinate to Co^{3+} to form $CoSb_6$ octahedra. These octahedra either share their vertices via one Sb atom or via one bond of the Sb_4 ring.

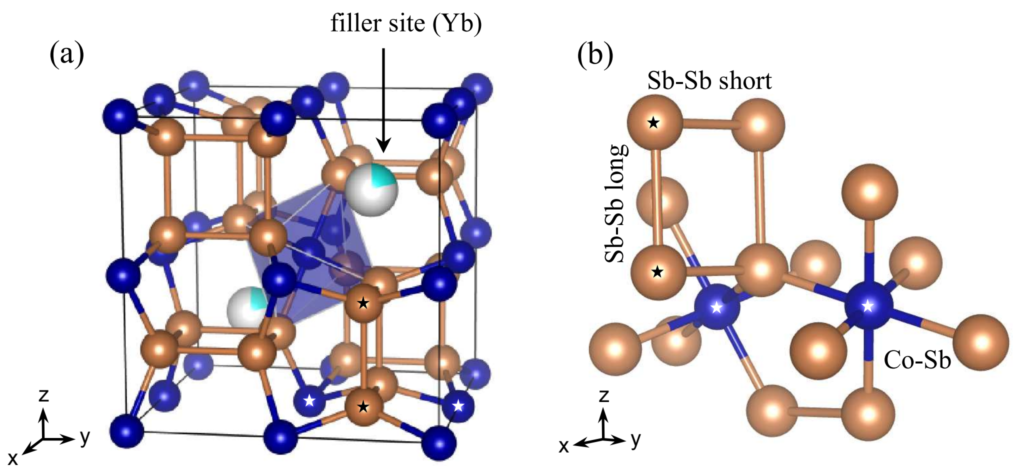

Figure 1: (a) Structural representation of Yb-filled $CoSb_3$ (shown with the origin shifted by $-\frac{1}{4}[111]$) with Co in blue, Sb atoms in gold, and Yb atoms (filler) in light blue. Sb forms Sb_4 rings that coordinate to Co. (b) Structural motif of $CoSb_3$. Two octahedra share either one Sb or an edge of an Sb-Sb ring. Star labeled atoms represent the motif (b) in context within the structure (a).

The skutterudite structure can be completely defined by its lattice parameter, *a*, and the position of the Sb atom (0, *y*, *z*). The different bond lengths illustrated in *Figure 1*a are then given as

$$d(Co-Sb)=a\left[\left(\frac{1}{4}\right)^2+\left(y-\left(\frac{1}{4}\right)\right)^2+\left(z-\left(\frac{1}{4}\right)\right)^2\right]^{\frac{1}{2}}, \qquad \text{Eq. 1}$$

$$d_1(Sb-Sb)=2az\,, \qquad \text{Eq. 2}$$

$$d_2(Sb-Sb)=a(1-2y)\,, \qquad \text{Eq. 3}$$

with d being the Co-Sb bond, d_1 the Sb-Sb short bond, and d_2 the Sb-Sb long bond[29]. As mentioned above, the Sb_4 ring contains two bond lengths given by Eq. 2 and Eq. 3 and a fixed bond angle of 90°. When $d_2 = d_1$ the *Oftedal relation* of $y + z = 0.5$ is met (named after the discoverer of the structure[30]), the ring is a perfect square. In addition, the $CoSb_6$ octahedra do not exhibit perfect O_h symmetry either. All bond lengths are equal but the bond angles are distorted from 90°. One of the most defining characteristics of this structure is the large cage centered at (0,0,0). This interstitial site is commonly referred to as the filler site and can be used to for chemical doping. The solubility limit of doping atoms on this filler site can be a limiting factor when optimizing the chemical potential of thermoelectrics, and it was recently highlighted that this solubility limit is temperature and composition dependent[31,32]. Interstitial doping atoms are weakly bonded to the cage structure and much effort has been devoted to understanding how lattice dynamics of this *rattling* atom affect the thermal properties of filled skutterudites[33–35].

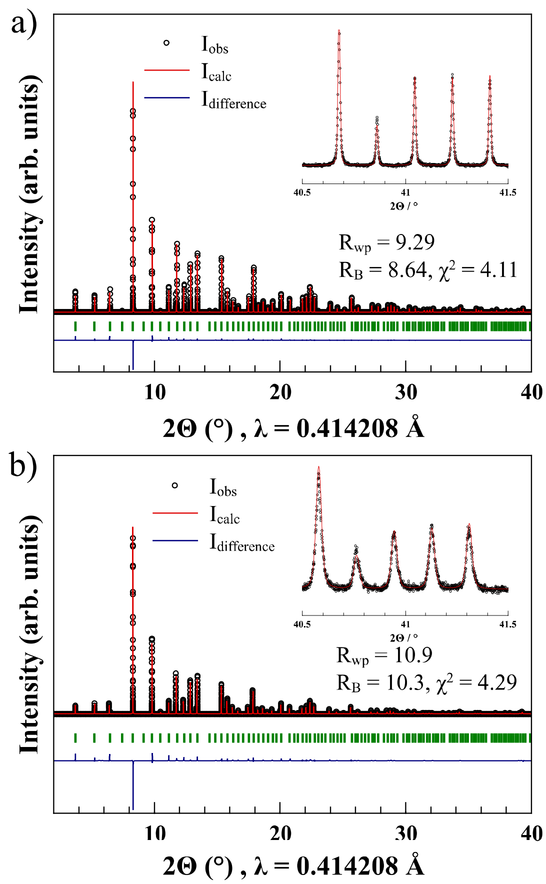

Figure 2: Exemplary refinement of (a) $CoSb_3$ and (b) $Yb_{0.3}Co_4Sb_{12}$ at 300 K with the corresponding profile residuals. The black circles are the experimental data, the red line is the calculated histogram, and the line below is the difference profile between the observed and calculated values. The insets show a zoomed in view on high angle reflections and the high quality fit of the refinement at the corresponding low d-spacing.

Thermal expansion effects. In this work, temperature dependent synchrotron X-ray diffraction has been performed to study the structural evolution of Yb filled and unfilled $CoSb_3$ at higher temperatures. Exemplary results obtained via Rietveld refinements of the synchrotron data for both $CoSb_3$ and $Yb_{0.3}Co_4Sb_{12}$ at 300 K can be found in *Figure 2*. The samples are all phase pure and good profile residuals can be obtained, indicating a high quality of the fit. All the relevant temperature dependent refinement data is tabulated in Table S1 and S2.

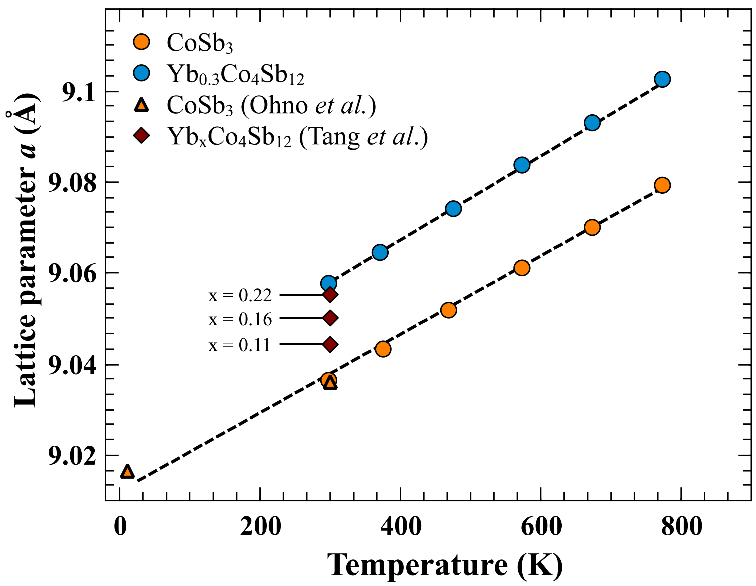

Figure 3: Temperature dependent lattice parameter of $CoSb_3$ obtained from the Rietveld refinements, showing the positive thermal expansion of the unit cell. Introduction of the filler atom further increases the unit cell. For comparison, data for increasing amounts of Yb are shown from Tang et al[32]*. Literature data from Ohno et al*[36] *show that the linear temperature dependence of a in $CoSb_3$ is maintained down to 10 K.*

Figure 3 shows the refined lattice parameter of $CoSb_3$, which increases linearly with increasing temperature. Introduction of the filler atom further increases the lattice and corresponds well with the expectation of Vegard's law within a $CoSb_3$ system, in which an increasing Yb content increases the lattice parameter linearly[32]. *Figure 4* shows the changes of the structural motif with increasing temperature. The y and z positions of Sb change with temperature (see Supporting Information), resulting in an increasing octahedral angle shifting towards a more symmetric regular O_h symmetry (*Figure 4*a). While the octahedra become more symmetric (90° angle), the increasing temperature drives the Sb_4 ring away from a square towards a more rectangular arrangement (*Figure*

*4*b). In addition to the temperature effects, the filler atom itself changes these relations. Filling the structure partially with Yb increases the octahedral distortion and increases the (y + z) relation towards a perfect square arrangement of the Sb_4 ring. Similar effects of substitution induced changing of bond angles have recently been reported in the $YbZn_2Sb_2$ Zintl phases[37].

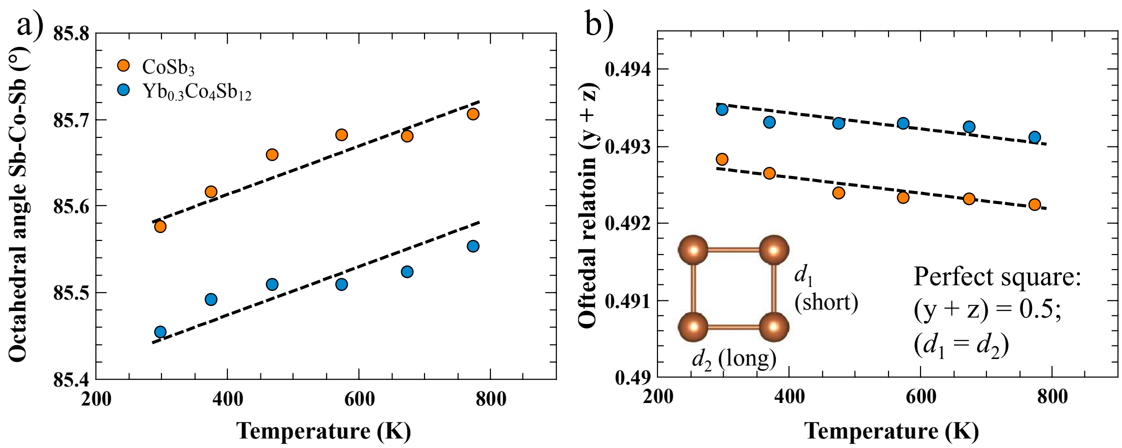

Figure 4: Changes in the $CoSb_6$ octahedral angle (a) and the Oftedal relation (b) with temperature. With increasing temperature, the structure shifts towards a more symmetric octahedron and away from a perfect square. Note that the doping with a filler atom leads to a distortion of the octahedral away from a symmetric 90° angle and a more square Sb_4 ring arrangement.

The atomic displacement parameters, $\langle u^2 \rangle$, obtained (Table S1 and S2) agree with what has been previously reported for $CoSb_3$[38], and other filled skutterudites[39]. The Yb atom has significantly larger values for $\langle u^2 \rangle$ than the Co and Sb atoms, which has been cited as evidence of the rattling nature of the Yb atom on this cage site[40]. The temperature dependence of $\langle u^2 \rangle$ gave an Einstein temperature for this localized mode of $\theta_E = 65(5)\ K$, which is similar to Yb in $YbFe_4Sb_{12}$[41].

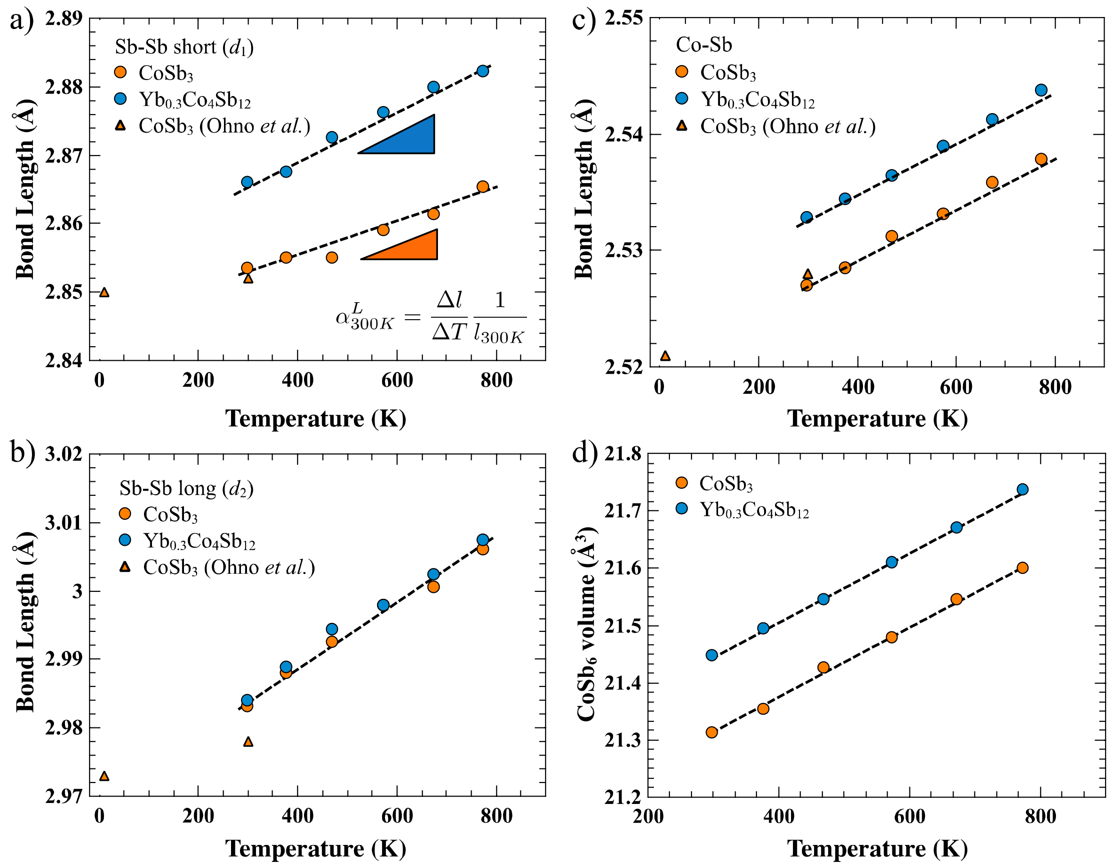

Figure 5: Temperature dependence of the Co-Sb (c) and Sb-Sb bond lengths (a) and (b). Lines correspond to linear fits used to calculate the local thermal expansion coefficient α^L_{300K}. Literature values from Ohno et al.[36] *are shown by triangles, showing the good fit of the data with literature values at room temperature and at 10K. While all bonds expand with increasing temperature in the undoped $CoSb_3$, the longer bond exhibits a larger slope and faster thermal expansion. Substitution with the filler atom increases the bond lengths as well. d) Temperature dependence of the octahedral volume, showing the linear thermal expansion of the $CoSb_6$ octahedra.*

Local thermal expansion coefficients. The changing Sb positions clearly affect the *Oftedal relation*, therefore the local chemical bonds, especially the Sb-Sb bonds within the Sb_4 ring, must be changing as well. *Figure 5* shows the temperature dependent evolution of the different bond lengths; the Co-Sb bond and the short and long Sb-Sb bonds, d_1 and d_2, respectively. At room temperature, the results correspond well with the structural data by Ohno *et al.*[36] While all bond lengths increase with temperature, as expected due to thermal expansion, differences in the slopes between the different bonds can be detected. In addition, differences in the bond lengths of the substituted samples can be seen as well. To assess these differences, the coefficient of thermal expansion (CTE) is calculated for each bond separately and is treated as a linear expansion coefficient defined as

$$\alpha_{300K}^{L} = \frac{\Delta l}{\Delta T}\frac{1}{l_{300K}}, \qquad \text{Eq. 4}$$

where Δl is the change in length, ΔT is the change in temperature, and l_{300K} is the length at 300 K. For a better understanding of the changes we will define α_{300K}^{L} for bond lengths as a *local*-CTE and the evolution of the lattice parameter as CTE. Temperature dependence ($\Delta l/\Delta T$) of the obtained structural parameters were successfully fit, giving α_{300K}^{L} through Eq. 4 and are shown in *Figure 5*. The values for the CTE and the *local*-CTE are tabulated in *Table 1*. The obtained values of the thermal expansion coefficients of the unit cell correspond well with other literature values. For instance, Rogl *et al.*[42] measured a CTE of $CoSb_3$ to be 9.1×10^{-6} K^{-1} via dilatometer measurements agreeing with our value in *Table 1*.

Table 1: Linear thermal expansion coefficients of the Sb-Sb, Co-Sb and Yb-Sb bonds in unfilled and filled skutterudite (normalized to the bond lengths at 300 K).

Structural parameter	$\boldsymbol{\alpha_{300K}^{L}}$ $(10^{-6}\ K^{-1})$	
	$CoSb_3$	$Yb_{0.3}Co_4Sb_{12}$
Lattice parameter, *a*	9.9	10.5
Sb-Sb long (d_2)	15.6	15.9
Sb-Sb short (d_1)	8.6	12.6
Co-Sb (d)	9.2	9.1
Yb-Sb	-	8.6

Figure 5 and *Table 1* show that the *local*-CTE (α_{300K}^{L}) of the long Sb-Sb bond in $CoSb_3$ is significantly larger than that of the Co-Sb and the short Sb-Sb bond. In other words, with increasing temperature the long Sb-Sb bond (d_2) expands much faster than the other two bonds. This faster increase of bong length of d_2 and the corresponding

slower increase of the short Sb-Sb bond (d_1) leads to the observed behavior of a structural shift towards a more rectangular Sb_4 ring.

Upon doping of $CoSb_3$ with Yb, the α^{L}_{300K} of the Sb-Sb short bond increases by nearly 50% while the α^{L}_{300K} for the Co-Sb and the Sb-Sb long bond remains essentially unchanged (*Figure 5*a). In addition, the length of the short Sb-Sb bond is significantly increased upon doping, while the length of Co-Sb bond is only slightly increased and that of the long Sb-Sb bond remains unchanged (see *Figure 5*). The size of the filler atom and the resulting change in lattice parameter cannot account for the different changes of the local bonding nature, as a typical Vegard behavior is supposed to change the lattice and the atomic positions in a similar manner. These data clearly show the qualitative differences in the chemical nature of the two Sb-Sb bonds in $CoSb_3$. Differences of these two chemical bonds has already been reported by Ohno *et al.*[36] using the maximum entropy method to reveal differences in the electron density between the Sb-Sb long and Sb-Sb short bonds. The electron density between the short bond was larger (by about 30%) than that between the long bond. This agrees well with the data presented here; less electron density results in a weaker bond, which should have a larger thermal expansion coefficient than a bond with more electron density between the atoms. In addition, calculations via density functional theory on the $CoSb_3$ lattice under strain showed that the Sb-Sb long bond was the first to break under a shear stress, which also support these experimental results[23]. From these structural data one may speculate the reason for the differences in the *local*-CTE behavior between the doped and undoped $CoSb_3$. The filler atom leads to an elongation of the short Sb-Sb bond and hence less bonding interaction and lower bond order[47] for the Sb-Sb bond (see *Figure 5*) and with it a much faster thermal expansion similar to the long Sb-Sb bond.

The differences in the bonds local thermal expansion coefficients as well as the differently affected bond length after substitution with the filler atom are somewhat unexpected results. To provide an explanation, we will consider the inherent bonding interactions using a molecular orbital theory approach and the changes in the electronic band structure are examined via density functional theory.

3.2 Band structure of doped and undoped $CoSb_3$

A chemical understanding of the electronic band structure. As recently shown for Zintl compounds[43], a combined approach using molecular orbital (MO) diagrams and density function theory can help gain a better understanding of the underlying chemical nature of the bands and how changes in structure and Fermi level may affect the bonding and electronic band situation. To interpret the observed thermal expansion behavior, we first attempt to understand the bonding qualitatively using a molecular orbital approach to determine the character of the valence and conduction bands. We then compare these conclusions to Crystal Orbital Hamilton Population (COHP) and density of states calculations.

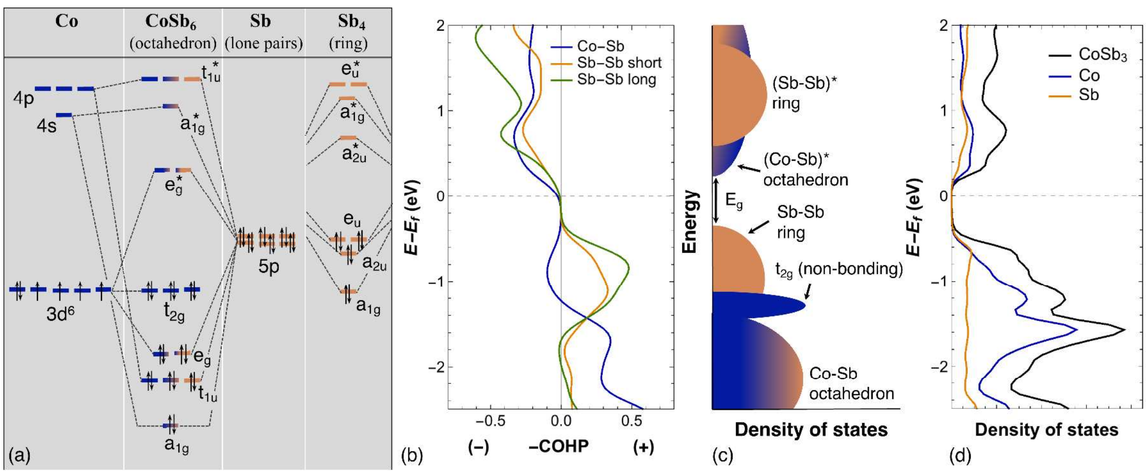

Figure 6: In all panels, blue corresponds to contributions from Co and orange to contributions from Sb. a) Molecular orbital diagrams of the $CoSb_6$ octahedron and the Sb_4 ring. Atomic orbitals are not shown for the Sb_4 ring. The octahedral crystal field splitting is visible and gives, in combination with the bonding, anti-bonding separation of the Sb-Sb bonds the band gap. b) Crystal Orbital Hamilton Population (COHP) calculated from the DFT data shown in Figure 7a, showing the bonding nature of the Sb-Sb bonds in the valence bands and Sb-Sb anti-bonding states in the conduction band. The Co-Sb bonds in the valence band are predominantly non-bonding (t_{2g}) in nature, whereas the conduction band has anti-bonding Co-Sb contributions. c) Schematic DOS estimated from MO diagrams in (a). d) Partial, atom projected DOS calculated from DFT data shown in Figure 7a.

*Figure 6*a shows the molecular orbitals for a $CoSb_6$ octahedron in which the Sb lone pairs of the Sb_4 ring coordinate to Co^{3+} forming an octahedral crystal field. The molecular orbital shows the octahedral crystal field splitting between the t_{2g} and e_g

orbitals. Co^{3+} exhibits six *d*-electrons (d^6 configuration) and therefore, the filled non-bonding t_{2g} orbitals express themselves as heavy states in the density of states of the valence band.[43] The filled deeper energy levels (a_{1g}, t_{1u} and e_g) in the valence band are of bonding nature and the empty anti-bonding states form the conduction band, with e_g^* representing the conduction band minimum[44]. *Figure 6*b shows the COHP of the different bonds and confirms the nature of low lying bonding Co-Sb states, the non-bonding t_{2g} closer to the valence band maximum and anti-bonding states at the conduction band edge. *Figure 6*a shows the molecular orbital diagram of a hypothetical Sb^{-1}–Sb^{-1} 4-member ring in D_{4h} symmetry (square arrangement), with the electronic configuration of a Sb with two bonds, *i.e.* valence of -1 using Zintl valence counting.

This molecular orbital diagram represents an oversimplification of the real electronic arrangement; for one the Sb_4 ring is rectangular and therefore D_{2h} symmetry and also a rigorous description of the molecular orbitals of the Sb_4^{4-} unit would need to account for all 4 states/atom not only the two shown here. For simplicity, we have chosen this single Sb-Sb bond in which the symmetry of the square and the corresponding electronic energy levels[45], as well as the electron count for Sb^{-1} with two bonds and two lone pairs incorporated. A deeper discussion regarding the contribution of the polyanionic ring to the skutterudite band structure, as well as a full tight-binding calculation, can be found in reference[46]. For a more in depth discussion on the bands and energetic configurations in solids with square arrangements, the reader is referred to Tremel and Hoffmann[45]. While the difference in symmetry between D_{4h} to D_{2h} will shift (and potentially split) the energy levels, the qualitative nature of the bonding states in the valence and anti-bonding states in the conduction band will be unaltered as can be seen in the COHP. In brief, the Sb-Sb bonding arrangement will result in bands with square-ring bonding character at the top of the valence band and bands with square-ring anti-bonding character near, but not exactly at, the bottom of the conduction band.

While the *s* and p_z orbitals of Sb^{-1} can mix with the *s*, p_z, d_{z2} and d_{x2-y2} of the metal at the Γ point (i.e. the lone pairs coordinate to Co to form $CoSb_6$ octahedra) the bonding orbitals of the Sb_4 ring cannot significantly mix with the $CoSb_6$ octahedron as they do not have the correct topology with the Co *3d*-orbitals in the D_{3d} point group[45,46]. In other words, at the Γ point we can neglect the interaction of the Sb_4^{4-} ring molecular orbitals with the $CoSb_6$ octahedron and the electronic structure of Sb_4^{4-} will superimpose on top of this $CoSb_6$ molecular orbital diagram. The bonding states of the Sb_4 ring are at a similar energy level as the t_{2g} nonbonding orbitals of Co character requiring DFT calculations to place them in the correct order. This makes the valence band edge of $CoSb_3$ primarily Sb-Sb bonding character. The Sb_4 anti-bonding states are located slightly above the e_g^* anti-bonding states of Co character, as confirmed by the calculated partial density of states (*Figure 6*d). Following this, we conclude that the primary conduction band CB_Γ can be attributed to the Co-Sb anti-bonding states, as has previously been established by Luo *et al*[44]. The secondary conduction band, CB_2, could then be of Sb-Sb anti-bonding character.

Band convergence with n-type doping. Using the structural data of Section 3.1, the electronic band structures were calculated and the results at 300 K are given in *Figure 7*. Results at higher temperatures are shown in Figure S3 and reveal how lattice expansion influences the band structure (neglecting lattice vibrations and the electron-phonon interaction). The band structure shows a direct band gap at the Γ point and an additional secondary conduction band (CB_2) at higher energies. The extraordinary thermoelectric properties of n-type filled $CoSb_3$ have recently been attributed to contributions from this secondary conduction band. At higher temperatures and when n-type doped, carrier transport seems to occur in both bands, resulting in a higher valley degeneracy and higher thermopower[15]. An understanding of the chemical nature of the bands and how they change with temperature and chemical doping are of critical importance when optimizing *n*-type $CoSb_3$. To elucidate the effect of the doping on the $CoSb_3$ band structure, DFT calculations were conducted on supercell structures with Yb atoms included on the filler site representing a composition of $Yb_{0.25}Co_4Sb_{12}$.

Because the calculations were conducted on supercell structures the Brillouin zone size was reduced, resulting in a folding of the bands. To compare these band structures to that of undoped $CoSb_3$ (primitive cell), the band structures were unfolded and are shown in *Figure 7*b (effective primitive cell band structure). The two conduction bands become closer in energy with Yb doping as observed in *Figure 7*, where by aligning energy scales at the bottom of $CB_{\Gamma,}$ a decrease in the energy of the band offset ($CB_2 - CB_\Gamma$) is shown. This band convergence was also observed in the calculations of Shi *et al.*[16] in which a different, higher conduction band (at Γ in the supercell), was highlighted as opposed to the CB_2 discussed here. It can also be seen that the Fermi level is increased to just above the CB_2 minimum, confirming the contribution of this band to electrical transport in *n*-type doped $CoSb_3$. The band between the Γ and P point also moves quickly upon the addition of filler atoms,[16] which is associated with the movement of the CB_2 and addition of Yb.

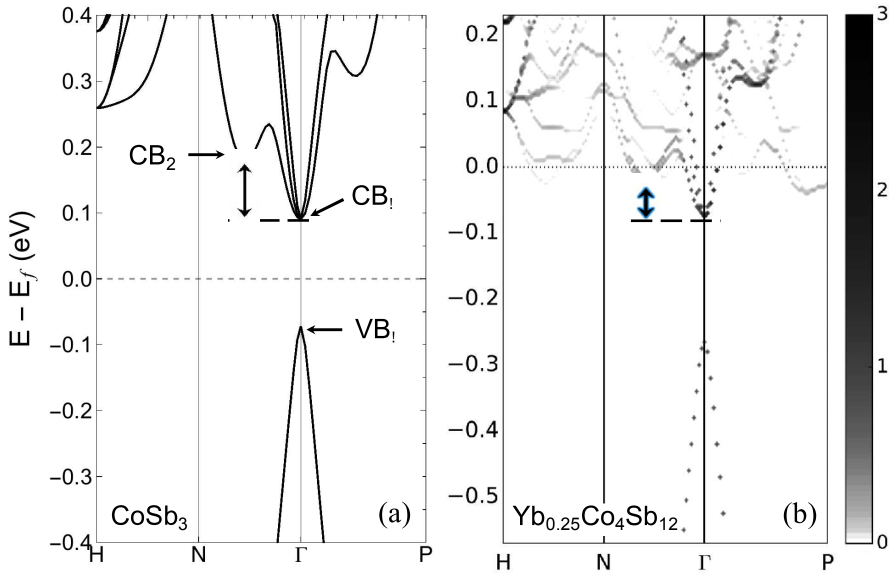

Figure 7: a) Calculated band structure of undoped $CoSb_3$ at 300 K with the relevant band extrema labeled. The valence band maximum and conduction band minimum are at the Γ point (3-fold degenerate), making $CoSb_3$ a direct band gap semiconductor. At higher energies, there is a second conduction band with 12 carrier pockets (CB_2). b) Effective primitive cell band structure of Yb-doped $CoSb_3$ calculated using a supercell (with fixed structural parameters). Dashed lines and color-coded arrows are guides to the eye, showing that in the doped structure the conduction bands are shifted compared to the undoped E(k). The scale bar represents the weighting function.

In these calculations, the introduction of Yb on the filler cage site can influence the band structure in several ways. When introduced, the Yb atom will simultaneously change the potential field set by the nuclei of the lattice (lattice potential effect) and increase the number of electrons in the system (carrier density effect). Therefore, to truly know the origin of band convergence, one needs to determine which of these effects is most responsible for the changes in band structure observed from *Figure 7*a to *Figure 7*b, namely the decrease of ($CB_2 - CB_\Gamma$). To achieve this, an additional calculation was conducted on $CoSb_3$ with additional electrons introduced to simulate the electrons donated with Yb doping, but without the associated change in the lattice potential field.

The result of this calculation is shown in *Table 2*, and reveals that a decrease in ($CB_2 - CB_\Gamma$), an increase in E_g, and a slight increase of the Sb-Sb short bond all occur when the Fermi level is increased. Charged impurity calculations of $Yb_{0.25}Co_4Sb_{12}$ with Yb_i^{2+} on the interstitial site, simulating a removal of the conduction electrons donated by Yb, show similar trends. In *Table 2* $CoSb_3$: doped refers to the addition of four electrons (per 2x2x2 supercell) and $Yb_{0.25}Co_4Sb_{12}$: doped refers to Yb_i^0 as the interstitial defect, undoped refers to Yb_i^{2+}. The position-relaxed calculations show that upon doping with Yb, Sb-Sb short and Co-Sb bonds increase while the Sb-Sb long bond is essentially unchanged, agreeing with the diffraction data (see *Figure 5*). Through this analysis, we suggest that the filler atom changes the local structure leading to changes in bonding interactions resulting in what may have been unexpected trends in bond lengths and *local*-CTE, as discussed above. Additionally, the slight change in crystal structure with increased E_f demonstrates a coupling of it with these electronic states.

While the addition of Yb leads to the observed structural changes and with it changes in the band structure, the increasing Fermi level due to a donation of electrons into the conduction band and occupation of anti-bonding states (see *Figure 6*) further lowers the secondary energy gap ($CB_2 - CB_\Gamma$). These results suggest that band convergence in n-type $CoSb_3$ can be induced by increasing the *carrier density*, and therefore should happen with all types of n-type dopants (e.g. other rare earth fillers, alkaline earth and alkali metal fillers, as well as Te or Ni doping).

Tang *et al*.[15] constructed a three-band model within the rigid band approximation, with a band offset of ($CB_2 - CB_\Gamma$) = 0.8 eV, which is between the values we obtained for $CoSb_3$ and $Yb_{0.25}Co_4Sb_{12}$. This model successfully predicted the experimentally observed change in density of states effective mass (obtained via Seebeck measurements). The change in ($CB_2 - CB_\Gamma$) observed here is a higher order effect that would not alter the qualitative conclusions of Tang.

Simply stated, Yb doping induces structural changes and increases carrier density populating anti-bonding states both of which affect the electronic band structure. This mechanism for obtaining band convergence is different than other approaches in thermoelectric materials, such as changing band dispersion in PbTe[2,7,9,10], and has not been observed before.

*Table 2: DFT calculations with different Fermi levels, and computational parameters. Similar changes in the band structure and structural parameters are observed with 'doping' regardless of computational method. *Indicates that this calculation is shown in Figure 7. †Indicates that the values are average bond distances within the supercell.*

Description				**Band structure**		**Structural parameters**		
Composition	doped/ undoped	*a*	positions	E_g (eV)	$CB_2 - CB_\Gamma$ (eV)	Sb-Sb short (Å)	Sb-Sb long (Å)	Co-Sb (Å)
$CoSb_3$*	undoped	fixed	fixed	0.163	0.089	2.854	2.983	2.527
$CoSb_3$	doped	fixed	fixed	0.215	0.077	2.854	2.983	2.527
$CoSb_3$	undoped	fixed	relaxed	0.242	0.105	2.882	3.014	2.518
$CoSb_3$	doped	fixed	relaxed	0.292	0.093	2.884	3.013	2.518
$Yb_{0.25}Co_4Sb_{12}$*	doped	fixed	fixed	0.191	0.050	2.866	2.984	2.533
$Yb_{0.25}Co_4Sb_{12}$	undoped	fixed	relaxed	0.221	0.088	2.898†	3.012†	2.524†
$Yb_{0.25}Co_4Sb_{12}$	doped	fixed	relaxed	0.272	0.075	2.900†	3.012†	2.523†

4. Conclusion

The thermal expansion behavior of bonds (*local*-CTE) within Yb-filled and unfilled $CoSb_3$ has been studied with temperature-dependent synchrotron diffraction, revealing a difference in the chemical nature of the Sb-Sb long and short bonds. Specifically, the Sb-Sb long bond is found to have a significantly larger thermal expansion than the Sb-Sb short, and Co-Sb bonds. By combining these structural results with systematic density functional theory calculations and molecular orbital diagrams, the chemical nature of band structure features was determined. It was identified that upon n-type doping, the charge carriers introduced populate anti-bonding states and change the electronic structure, leading to band convergence at room temperature in electron doped $CoSb_3$. Computational results on Yb-doped $CoSb_3$ agree with diffraction data showing that occupying the filler site changes the local structure in addition to simple lattice expansion. This work shows that the introduction of charge carriers, from presumably any n-type dopant, can influence the electronic structure and lead to band convergence.

We show the importance of combining accurate structure determination with systematic density functional theory calculations to understand band convergence and structural changes in thermoelectric materials. This combined approach is a powerful tool that can provide new strategies and approaches in optimizing energy materials.

ASSOCIATED CONTENT

Supporting Information

Tables of the refined temperature dependent structural parameters and refinement statistics, obtained from Rietveld refinements against synchrotron diffraction data, their corresponding diffraction pattern as well as the resulting calculated band structures at different temperatures can be found here. Furthermore, comparisons of bond lengths calculated with the Yb dopant with and without electrons added, as well a comparison of calculated band offsets are given. The temperature dependence of the band gap and band offset is given as well as information about the thermal expansion behavior and Einstein temperature. This material is available free of charge via the Internet at http://pubs.acs.org.

AUTHOR INFORMATION

Corresponding Authors

*jeff.snyder@northwestern.edu; *wolfgang.g.zeier@phys.chemie.uni-giessen.de

Notes

The authors declare no competing financial interests.

ACKNOWLEDGMENT

G.J.S and R.H. acknowledge the EFRC Solid-State Solar-Thermal Energy Conversion Center (S3TEC) award number DE-SC0001299. The authors acknowledge the use of the Advanced Photon Source at Argonne National Laboratory for the synchrotron diffraction data, as supported by the U.S. Department of Energy, Office of Science, Office of Basic Energy Sciences, under Contract No. DE-AC02-06CH11357. W.G.Z acknowledges financial support provided by the DFG via the GrK (Research training group) 2204 "Substitute Materials for sustainable Energy Technologies as well as the Funds of the Chemical Industry (FCI).

References

(1) Tan, G.; Zhao, L. D.; Shi, F.; Doak, J. W.; Lo, S. H.; Sun, H.; Wolverton, C.; Dravid, V. P.; Uher, C.; Kanatzidis, M. G. High Thermoelectric Performance of P-Type SnTe via a Synergistic Band Engineering and Nanostructuring Approach. *J. Am. Chem. Soc.* **2014**, *136*, 7006–7017.

(2) Pei, Y.; Shi, X.; LaLonde, A.; Wang, H.; Chen, L.; Snyder, G. J. Convergence of Electronic Bands for High Performance Bulk Thermoelectrics. *Nature* **2011**, *473*, 66–69.

(3) Pei, Y.; Wang, H.; Snyder, G. J. Band Engineering of Thermoelectric Materials. *Adv. Mater.* **2012**, *24*, 6125–6135.

(4) LaLonde, A. D.; Pei, Y.; Wang, H.; Jeffrey Snyder, G. Lead Telluride Alloy Thermoelectrics. *Mater. Today* **2011**, *14*, 526–532.

(5) Bozin, E. S.; Malliakas, C. D.; Souvatzis, P.; Proffen, T.; Spaldin, N. A.; Kanatzidis, M. G.; Billinge, S. J. L. Entropically Stabilized Local Dipole Formation in Lead Chalcogenides. *Science.* **2010**, *330*, 1660–1663.

(6) Zeier, W. G.; Zevalkink, A.; Gibbs, Z. M.; Hautier, G.; Kanatzidis, M. G.; Snyder, G. J. Thinking Like a Chemist: Intuition in Thermoelectric Materials. *Angew. Chemie Int. Ed.* **2016**, 6826–6841.

(7) Biswas, K.; He, J.; Blum, I. D.; Chun-I, W.; Hogan, T. P.; Seidman, D. N.; Dravid, V. P.; Kanatzidis, M. G. High-Performance Bulk Thermoelectrics with All-Scale Hierarchical Architectures. *Nature* **2012**, *489*, 414–418.

(8) Pei, Y.; LaLonde, A. D.; Heinz, N. A.; Shi, X.; Iwanaga, S.; Wang, H.; Chen, L.; Snyder, G. J. Stabilizing the Optimal Carrier Concentration for High Thermoelectric Efficiency. *Adv. Mater.* **2011**, *23*, 5674–5678.

(9) Wang, H.; Gibbs, Z. M.; Takagiwa, Y.; Snyder, G. J. Tuning Bands of PbSe for Better Thermoelectric Efficiency. *Energy Environ. Sci.* **2014**, *7*, 804.

(10) Lee, Y.; Lo, S.; Androulakis, J.; Wu, C.-I.; Zhao, L.-D.; Chung, D.-Y.; Hogan, T. P.; Dravid, V. P.; Kanatzidis, M. G. High-Performance Tellurium-Free Thermoelectrics: All-Scale Hierarchical Structuring of p−Type PbSe−MSe Systems (M = Ca, Sr, Ba). *J. Am. Chem. Soc.* **2013**, *135*, 5152–5160.

(11) Zhang, J.; Liu, R.; Cheng, N.; Zhang, Y.; Yang, J.; Uher, C.; Shi, X.; Chen, L.; Zhang, W. High-Performance Pseudocubic Thermoelectric Materials from Non-Cubic Chalcopyrite Compounds. *Adv. Mater.* **2014**, *26*, 3848–3853.

(12) Zhu, H.; Sun, W.; Armiento, R.; Lazic, P.; Ceder, G. Band Structure Engineering through Orbital Interaction for Enhanced Thermoelectric Power Factor. *Appl. Phys. Lett.* **2014**, *104*, 82107.

(13) Liu, W.; Tan, X.; Yin, K.; Liu, H.; Tang, X.; Shi, J.; Zhang, Q.; Uher, C. Convergence of Conduction Bands as a Means of Enhancing Thermoelectric Performance of N-Type Mg_2Si_{1-x}. *Phys. Rev. Lett.* **2012**, *108*, 166601.

(14) Zeier, W. G.; Zhu, H.; Gibbs, Z. M.; Ceder, G.; Tremel, W.; Snyder, G. J. Band Convergence in the Non-Cubic Chalcopyrite Compounds Cu_2MGeSe_4. *J. Mater. Chem. C* **2014**, *2*, 10189–10194.

(15) Tang, Y.; Gibbs, Z. M.; Agapito, L. A.; Li, G.; Kim, H.-S.; Nardelli, M. B.; Curtarolo, S.; Snyder, G. J. Convergence of Multi-Valley Bands as the Electronic Origin of High Thermoelectric Performance in $CoSb_3$ Skutterudites. *Nat. Mater.* **2015**, *14*, 1223–1228.

(16) Shi, X.; Yang, J.; Wu, L.; Salvador, J. R.; Zhang, C.; Villaire, W. L.; Haddad, D.; Yang, J.; Zhu, Y.; Li, Q. Band Structure Engineering and Thermoelectric Properties of Charge-Compensated Filled Skutterudites. *Sci. Rep.* **2015**, *5*, 14641.

(17) Von Dreele, R.; Suchomel, M.; Toby, B. Advanced Photon Source: Compute X-ray Absorption http://11bm.xray.aps.anl.gov/absorb/absorb.php.

(18) Cromer, D. T.; Liberman, D. A. Anomalous Dispersion Calculations near to and on the Long-Wavelength Side of an Absorption Edge. *Acta Crystallogr. Sect. A* **1981**, *37*, 267–268.

(19) Larson, A. C.; Von Dreele, R. B. General Structure Analysis System (GSAS). *Los Alamos Natl. Lab. Rep.* **2004**, *LAUR 86-74*.

(20) Toby, B. H. "EXPGUI", a Graphical User Interface for GSAS. *J. Appl. Crystallogr.* **2001**, *34*, 210–213.

(21) Kresse, G.; Joubert, D. From Ultrasoft Pseudopotentials to the Projector Augmented-Wave Method. *Phys. Rev. B* **1999**, *59*, 1758–1775.

(22) Perdew, J. P.; Burke, K.; Ernzerhof, M. Generalized Gradient Approximation

Made Simple. *Phys. Rev. Lett.* **1996**, *77*, 3865–3868.

(23) Li, G.; Bajaj, S.; Aydemir, U.; Hao, S.; Xiao, H.; Goddard, W. A.; Zhai, P.; Zhang, Q.; Snyder, G. J. P-Type Co Interstitial Defects in Thermoelectric Skutterudite $CoSb_3$ Due to the Breakage of Sb_4-Rings. *Chem. Mater.* **2016**, *28*, 2172–2179.

(24) Tang, Y.; Qiu, Y.; Xi, L.; Shi, X.; Zhang, W.; Chen, L.; Tseng, S.-M.; Chen, S.; Snyder, G. J. Phase Diagram of In–Co–Sb System and Thermoelectric Properties of In-Containing Skutterudites. *Energy Environ. Sci.* **2014**, *7*, 812–819.

(25) Sofo, J. O.; Mahan, G. D. Electronic Structure of $CoSb_3$: A Narrow-Band-Gap Semiconductor. *Phys. Rev. B* **1998**, *58*, 15620–15623.

(26) Gibbs, Z. M.; Kim, H.; Wang, H.; White, R. L.; Drymiotis, F.; Kaviany, M.; Jeffrey Snyder, G. Temperature Dependent Band Gap in PbX (X=S, Se, Te). *Appl. Phys. Lett.* **2013**, *103*, 262109.

(27) Dronskowski, R.; Bloechl, P. E. Crystal Orbital Hamilton Populations (COHP): Energy-Resolved Visualization of Chemical Bonding in Solids Based on Density-Functional Calculations. *J. Phys. Chem.* **1993**, *97*, 8617–8624.

(28) Medeiros, P. V. C.; Stafstrom, S.; Bjork, J. Effects of Extrinsic and Intrinsic Perturbations on the Electronic Structure of Graphene: Retaining an Effective Primitive Cell Band Structure by Band Unfolding. *Phys. Rev. B - Condens. Matter Mater. Phys.* **2014**, *89*, 041407.

(29) Uher, C. Skutterudites : Prospective Novel Thermoelectrics. *Semicond. Semimetals* **2001**, *69*, 139–253.

(30) Oftedal, I. The Crystal Structure of Skutterudite and Related Minerals. *Nor. Geol. Tidsskr.* **1926**, *8*, 250–257.

(31) Tang, Y.; Hanus, R.; Chen, S.; Snyder, G. J. Solubility Design Leading to High Figure of Merit in Low-Cost Ce-$CoSb_3$ Skutterudites. *Nat. Commun.* **2015**, *6*, 7584.

(32) Tang, Y.; Chen, S.; Snyder, G. J. Temperature Dependent Solubility of Yb in Yb–$CoSb_3$ Skutterudite and Its Effect on Preparation, Optimization and Lifetime of Thermoelectrics. *J. Mater.* **2015**, *1*, 75–84.

(33) Möchel, A.; Sergueev, I.; Nguyen, N.; Long, G. J.; Grandjean, F.; Johnson, D. C.; Hermann, R. P. Lattice Dynamics in the $FeSb_3$ Skutterudite. *Phys. Rev. B* **2011**,

84, 64302.

(34) Chakoumakos, B. C.; Keppens, V.; Mandrus, D.; Sales, B. C.; Dai, P.; Coldea, R.; Maple, M. B.; Gajewski, D. A; Freeman, E. J.; Bennington, S. Localized Vibrational Modes in Metallic Solids. *Nature* **1998**, *395*, 876–878.

(35) Meisner, G. P.; Morelli, D. T.; Hu, S.; Yang, J.; Uher, C. Structure and Lattice Thermal Conductivity of Fractionally Filled Skutterudites: Solid Solutions of Fully Filled and Unfilled End Members. *Phys. Rev. Lett.* **1998**, *80*, 3551–3554.

(36) Ohno, A.; Sasaki, S.; Nishibori, E.; Aoyagi, S.; Sakata, M.; Iversen, B. B. X-Ray Charge Density Study of Chemical Bonding in Skutterudite $CoSb_3$. *Phys. Rev. B* **2007**, *76*, 64119.

(37) Zevalkink, A.; Zeier, W. G.; Cheng, E.; Snyder, J.; Fleurial, J.-P.; Bux, S. Nonstoichiometry in the Zintl Phase $Yb_{1-\delta}Zn_2Sb_2$ as a Route to Thermoelectric Optimization. *Chem. Mater.* **2014**, *26*, 5710–5717.

(38) Puyet, M.; Lenoir, B.; Dauscher, A.; Weisbecker, P.; Clarke, S. J. Synthesis and Crystal Structure of $Ca_xCo_4Sb_{12}$ Skutterudites. *J. Solid State Chem.* **2004**, *177*, 2138–2143.

(39) Sergueev, I.; Glazyrin, K.; Kantor, I.; McGuire, M. A.; Chumakov, A. I.; Klobes, B.; Sales, B. C.; Hermann, R. P. Quenching Rattling Modes in Skutterudites with Pressure. *Phys. Rev. B - Condens. Matter Mater. Phys.* **2015**, *91*, 2–8.

(40) Sales, B. C.; Chakoumakos, B. C.; Mandrus, D. Thermoelectric Properties of Thallium-Filled Skutterudites. *Phys. Rev. B* **2000**, *61*, 2475.

(41) Möchel, A.; Sergueev, I.; Wille, H. C.; Voigt, J.; Prager, M.; Stone, M. B.; Sales, B. C.; Guguchia, Z.; Shengelaya, A.; Keppens, V.; Hermann, R. P. Lattice Dynamics and Anomalous Softening in the $YbFe_4Sb_{12}$ Skutterudite. *Phys. Rev. B - Condens. Matter Mater. Phys.* **2011**, *84*, 184306.

(42) Rogl, G.; Zhang, L.; Rogl, P.; Grytsiv, A.; Falmbigl, M.; Rajs, D.; Kriegisch, M.; Müller, H.; Bauer, E.; Koppensteiner, J.; Schranz, W.; Zehetbauer, M.; Henkie, Z.; Maple, M. B. Thermal Expansion of Skutterudites. *J. Appl. Phys.* **2010**, *107*, 43507.

(43) Zeier, W. G.; Schmitt, J.; Hautier, G.; Aydemir, U.; Gibbs, Z. M.; Felser, C.; Snyder, G. J. Engineering Half-Heusler Thermoelectric Materials Using Zintl

Chemistry. *Nat. Rev. Mater.* **2016**, *1*, 16032.

(44) Luo, H.; Krizan, J. W.; Muechler, L.; Haldolaarachchige, N.; Klimczuk, T.; Xie, W.; Fuccillo, M. K.; Felser, C.; Cava, R. J. A Large Family of Filled Skutterudites Stabilized by Electron Count. *Nat. Commun.* **2015**, *6*, 6489.

(45) Tremel, W.; Hoffmann, R. Square Nets of Main Group Elements in Solid Materials. *J. Am. Chem. Soc.* **1987**, *109*, 124–140.

(46) Jung, D.; Whangbo, M. H.; Alvarez, S. Importance of the X_4 Ring Orbitals for the Semiconducting, Metallic, or Superconducting Properties of Skutterudites MX_3 and RM_4X_{12}. *Inorg. Chem.* **1990**, *29*, 2252–2255.

(47) Mulliken, R. S. Electronic Population Analysis on LCAO MO Molecular Wave Functions. I. *J. Chem. Phys.* **1955**, *23*, 1833.

TOC graphic

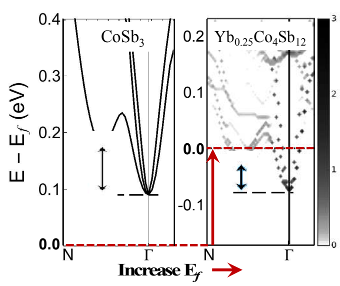

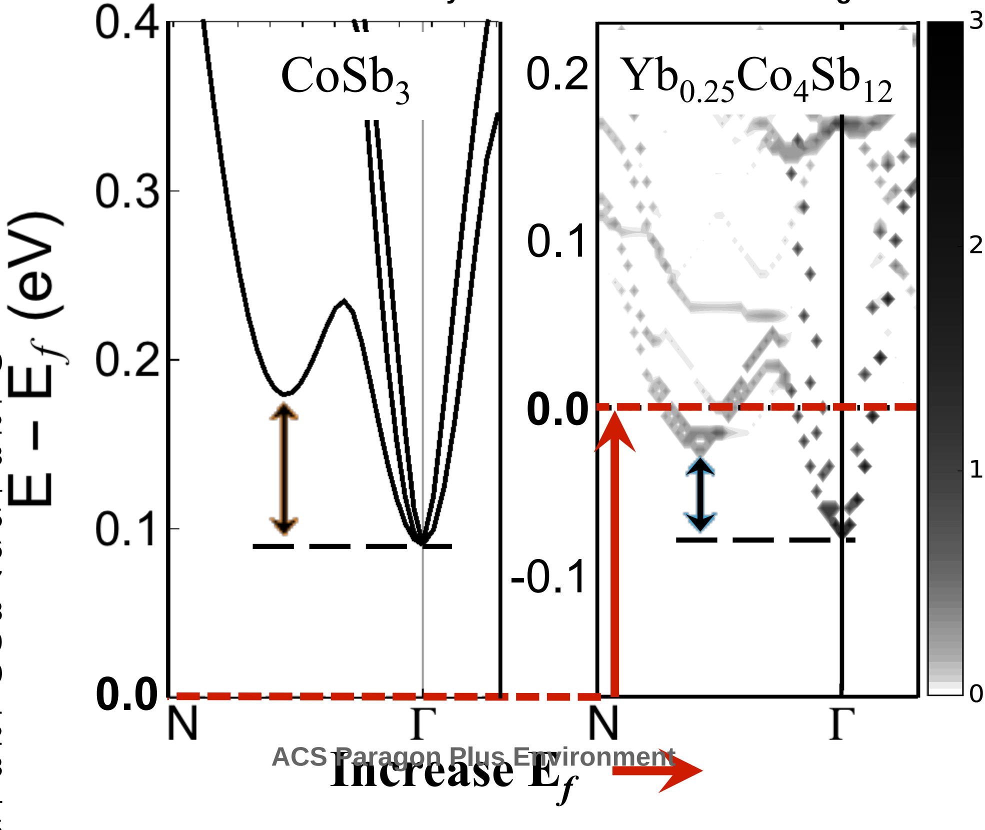
E - E_f (eV)
CoSb3
Yb0.25Co4Sb12
0.4
0.3
0.2
0.1
0.0
0.2
0.1
0.0
-0.1
N
Γ
N
Γ
3
2
1
0
Increase E_f